Electronic Supplementary Material (ESI) for Dalton Transactions.

Supporting Information

Electrochemical reduction of nitrite to ammonia on amorphous MoO_3 nanosheets

Tingting Wu [a], Fengyu Zhang [a], Jingxuan Wang [a], Xiaoxu Liu[a], Ye Tian [a], Ke Chu [b]**

[a] *College of Science, Hebei North University, Zhangjiakou 075000, Hebei, China*

[b] *School of Materials Science and Engineering, Lanzhou Jiaotong University, Lanzhou 730070, China*

**Corresponding author. wutingtinghnu@126.com (T.T. Wu), chuk630@mail.lzjtu.cn (K. Chu)*

Experimental Section

Synthesis of am-MoO_3

All chemicals were used as received without further purification. 0.24 g molybdenum metal powder was dissolved in 30 mL H_2O_2 aqueous solution. The solution was then transferred into the Teflon vessel and heated at 180 ^oC for 18 h. After cooling to room temperature, the resulting solution was then transferred into a supercritical CO_2 apparatus which was treated at 180 °C for 5 h under 10 MPa, the resulting products were collected by centrifuging, washing with deionized water/ethanol and drying under vacuum, obtaining am-MoO_3. For comparison, pristine MoO_3 was prepared by the same procedure without supercritical CO_2 treatment.

Electrochemical experiments

Electrochemical measurements were carried out using a CHI-760E electrochemical workstation employing a three-electrode cell system consisting of a am-MoO_3 working electrode, an Ag/AgCl reference electrode and a Pt foil counter electrode. All the potentials were referenced to a reversible hydrogen electrode (RHE) by the following equation: E (V vs. RHE) = E (V vs. Ag/AgCl) + 0.198 V + 0.059 × pH. Electrochemical NO_2RR measurements were conducted in an H-type electrochemical cell containing 0.5 M Na_2SO_4 with 0.1 M $NaNO_2$ separated by Nafion 211 membrane. Prior to use, the Nafion membrane was pretreated by heating it in a 5% H_2O_2 aqueous solution at 80 °C for 1 h, followed by rinsing with deionized water at 80 °C for another 1 h. After each chronoamperometry test for 0.5 h electrolysis at a specific potential, the liquid products were analyzed using colorimetric methods with UV-vis absorbance spectrophotometer (MAPADA P5), while the gas products were analyzed using gas chromatography (Shimadzu GC2010).

Determination of NH_3

The generated NH_3 was determined by an indophenol blue method[1]. Typically, 0.5 mL of electrolyte was extracted from the electrochemical reaction vessel and subsequently diluted tenfold with deionized water. Then 2 mL of diluted solution was removed into a clean vessel followed by sequentially adding NaOH solution (2 mL, 1 M) containing $C_7H_6O_3$ (5 wt.%) and $C_6H_5Na_3O_7$ (5 wt.%), NaClO (1 mL, 0.05 M),

and $C_5FeN_6Na_2O$ (0.2 mL, 1wt.%) aqueous solution. After incubation for 2 hours at room temperature. The mixed solution was measured in UV-Vis at 655 nm. The concentration-absorbance curves were calibrated using a range of concentrations in a standard NH_4Cl solution. Subsequently, the NH_3 yield rate and Faradaic efficiency (FE) were calculated using the following equation:

$$NH_3 \text{ yield} = (c \times V) / (17 \times t \times A) \quad (1)$$

Faradaic efficiency was calculated by the following equation:

$$FE = (5 \times F \times c \times V) / (17 \times Q) \times 100\% \quad (2)$$

where c (μg mL^{-1}) is the measured NH_3 concentration, V (mL) is the volume of electrolyte in the cathode chamber, t (s) is the electrolysis time and A is the surface area of CC (1×1 cm^2), F (96500 C mol^{-1}) is the Faraday constant, Q (C) is the total quantity of applied electricity.

Determination of N_2H_4

N_2H_4 in electrolyte was quantitatively determined by a Watt and Chrisp method[2]. To prepare the coloring solution, a combination of 300 mL C_2H_5OH, 5.99 g $C_9H_{11}NO$, and 30 mL HCl was mixed. Subsequently, 5 mL of the coloring solution was introduced to 5 mL of the electrolyte. After the incubation for 20 min at room temperature, the mixed solution was subjected to UV-vis measurement using the absorbance at 455 nm wavelength. The concentration-absorbance curve is calibrated by a series of concentrations of standard N_2H_4 solutions.

Characterizations

X-ray diffraction (XRD) pattern was performed on a Rigaku D/max 2400 diffractometer. Transmission electron microscopy (TEM), high-resolution transmission electron microscopy (HRTEM) and selected area electron diffraction (SAED) were carried out on a Tecnai G^2 F20 microscope. Electron paramagnetic resonance (EPR) measurements were recorded on a Bruker ESP-300 spectrometer.

Calculation details

DFT calculations were performed using a plane-wave technique with exchange-correlation interactions modeled by the Perdew-Burke-Ernzerhof (PBE) generalized gradient approximation (GGA) functional, as implemented in the Cambridge

sequential total energy package (CASTEP). The van der Waals interaction was described by using the DFT-D correction method. A cutoff energy of 450 eV was chosen and the 4×4×1 Monkhorst-Pack mesh was used in Brillouin zone sampling. The convergence tolerance was set to be 1.0×10^{-5} eV for energy and 0.02 eV $Å^{-1}$ for force. Crystalline MoO_3 (010) was modeled by a 4 × 4 supercell, and a vacuum region of 15 Å was used to separate adjacent slabs. Amorphous MoO_3 was built by relaxing the crystalline MoO_3 (010) at 500 K, and the ordered atomic arrangement could be damaged. am-MoO_3 was modeled by removing one surface O atom of amorphous MoO_3.

The free energies (ΔG, 298 K) for each reaction were given after correction:

$$\Delta G = \Delta E + \Delta ZPE - T\Delta S \quad (3)$$

where ΔE is the adsorption energy, ΔZPE is the zero-point energy difference and $T\Delta S$ is the entropy difference between the gas phase and adsorbed state.

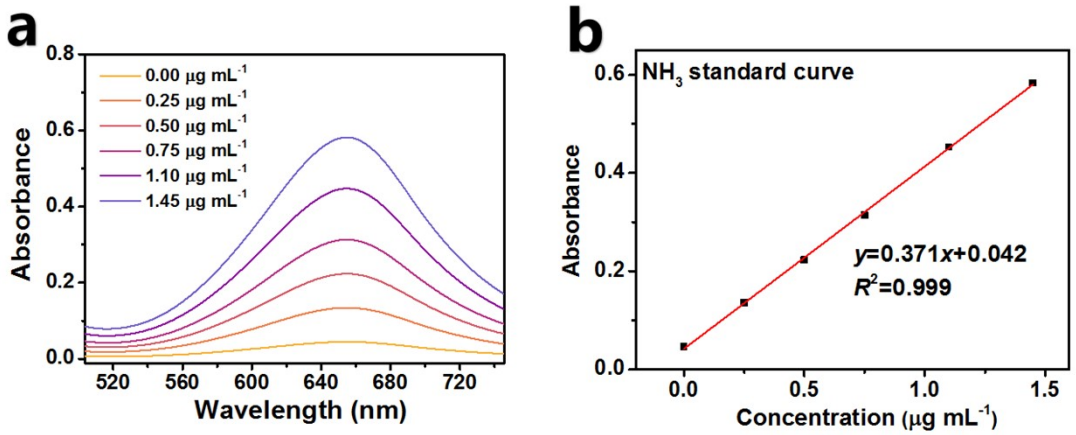

Fig. S1. (a) UV-vis absorption spectra of NH_4^+ assays after incubated for 2 h at ambient conditions. (b) Calibration curve used for the calculation of NH_3 concentrations.

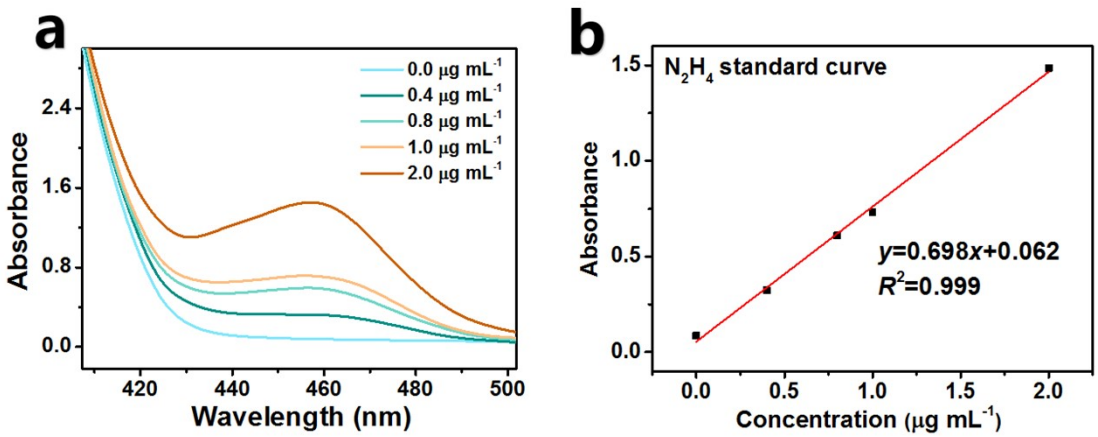

Fig. S2. (a) UV-vis absorption spectra of N_2H_4 assays after incubated for 20 min at ambient conditions. (b) Calibration curve used for calculation of N_2H_4 concentrations.

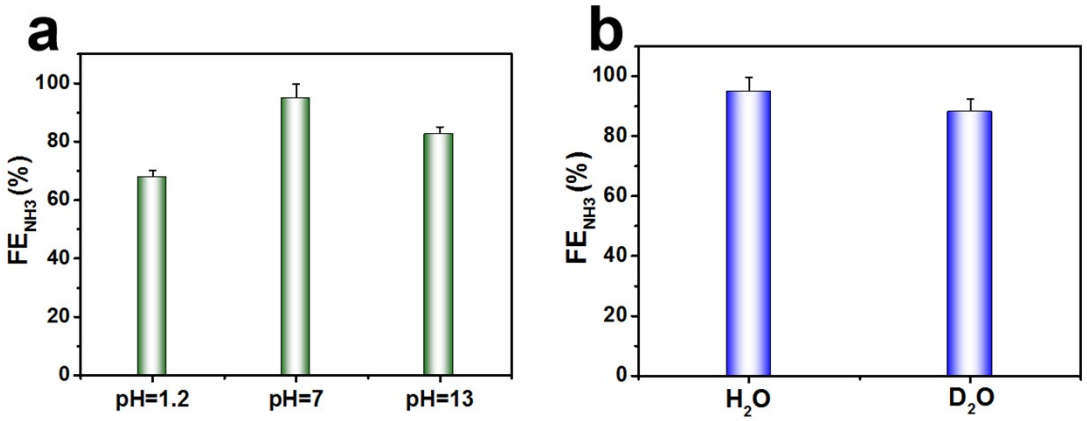

Fig. S3. Effects of (a) pH and (b) use of D_2O on FE_{NH3} of am-MoO_3 at -0.6 V.

It is seen in Fig. S3a that the neutral electrolyte (pH=7) facilitates the achievement of the high NO_2RR performance, while the performance is compromised in acidic (pH=1.2) and alkaline (pH=13) environments, especially in acidic electrolyte. This can be explained by that **(1)** at low pH, the competing HER would be enhanced and can greatly suppress the NO_2RR, while **(2)** at high pH, the available protons are too limited to provide the sufficient proton source for hydrogenating nitrogen species during the NO_2RR electrolysis, as electrocatalytic NO_2^--to-NH_3 conversion is known to be a hydrogenation process[3]. Regarding the influence of D_2O, it is seen in Fig. S3b that the use of D_2O instead of H_2O can slightly reduce the NO_2RR activity, which can be attributed to that the D-O bond of D_2O is more challenging to break during the catalytic reaction than H-O bond of H_2O[4]. Therefore, using D_2O as the solvent causes a lack of protons compared to H_2O as the solvent, leading to the compromised NO_2RR activity.

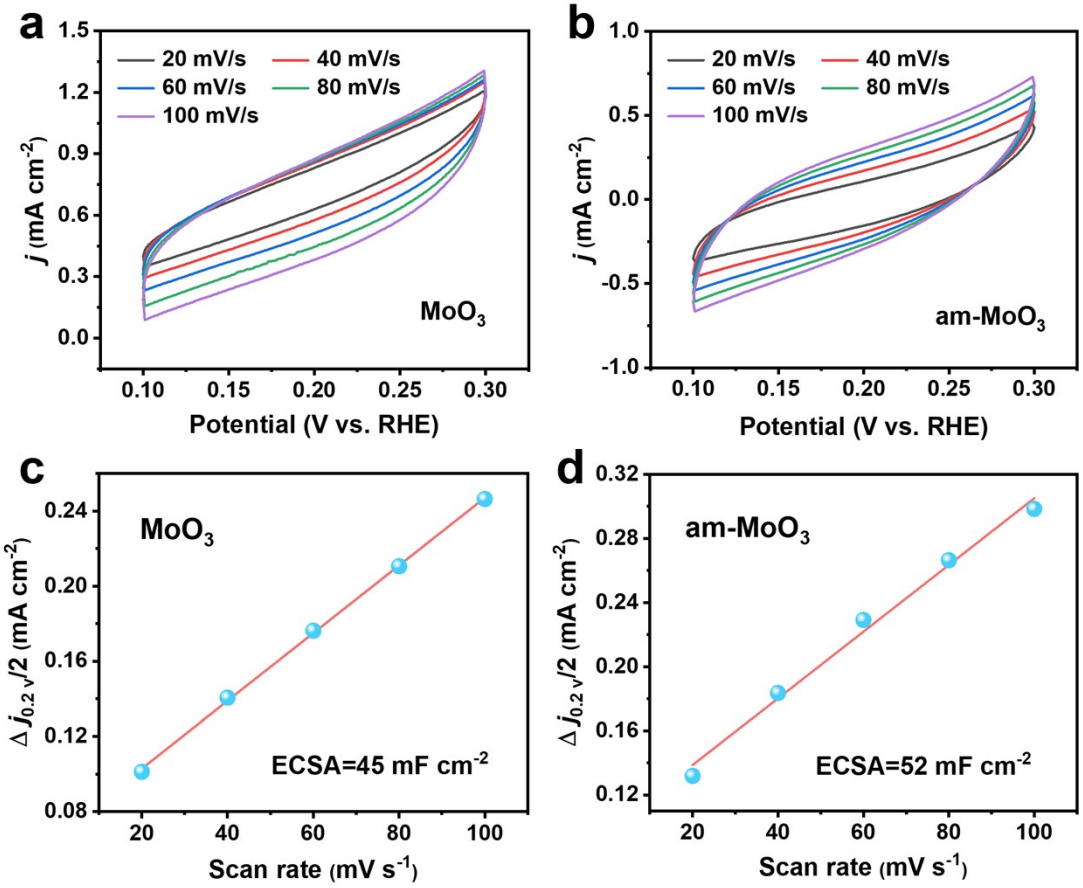

Fig. S4. CV measurements at different scanning rates for (a, c) MoO_3 and (b, d) am-MoO_3, and corresponding calculated ECSA.

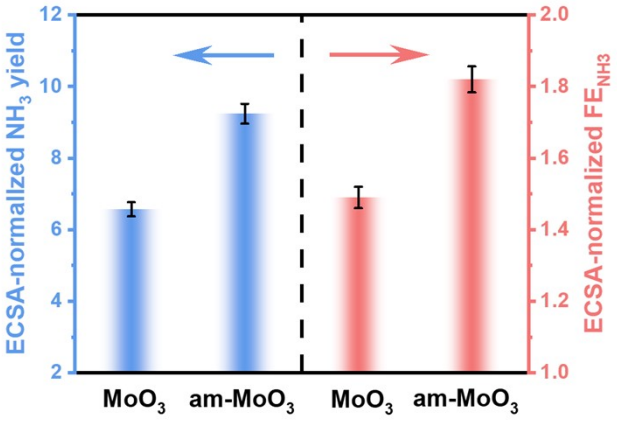

Fig. S5. Comparison of the ECSA-normalized NH_3 yield rates and FE_{NH3} between MoO_3 and am-MoO_3 at -0.6 V.

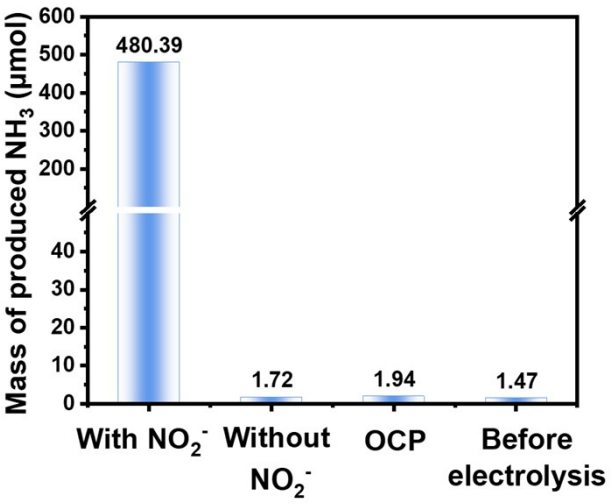

Fig. S6. Amounts of produced NH_3 on am-MoO_3 under different conditions: (1) electrolysis in NO_2^--containing solution at -0.6 V, (2) electrolysis in NO_2^--free solution at -0.6 V, (3) electrolysis in NO_2^--containing solution at open-circuit potential (OCP), (4) before electrolysis.

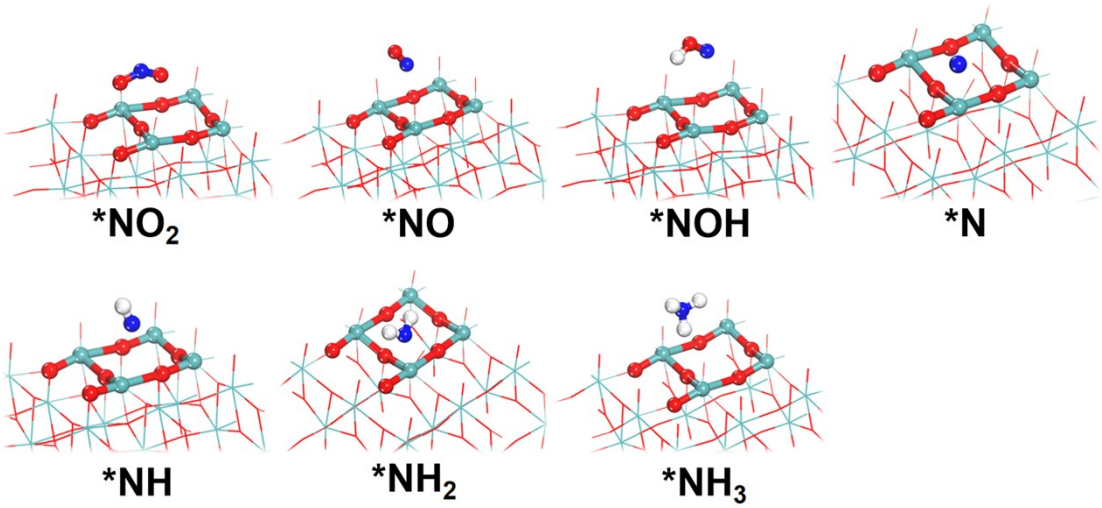

Fig. S7. Optimized structures of reaction intermediates on MoO_3.

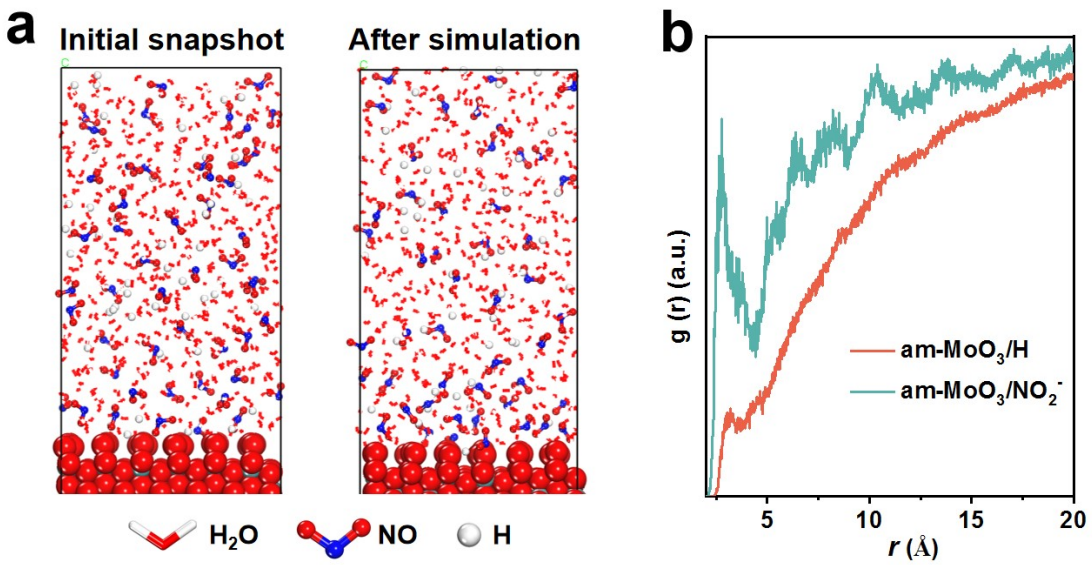

Fig. S8. (a) Initial and simulated snapshots for the dynamic process of NO_2^- and H on am-MoO_3, and their corresponding (b) RDF curves.

As shown in Fig. S8a, an obvious aggregation of NO_2^- on am-MoO_3 is observed after simulation. The calculated radial distribution function (RDF, Fig. S8b) curves show an enhanced am-MoO_3/NO_2^- interaction in comparison with am-MoO_3/H interaction[64], suggesting the preferred coverage of NO_2^- on am-MoO_3 than H.

Table S1. Comparison of the optimum NH_3 yield rate and NH_3-Faradic efficiency (FE_{NH3}) for the recently reported NO_2RR electrocatalysts at ambient conditions

Catalyst	Electrolyte	NH_3 yield rate ($mg\ h^{-1}\ cm^{-2}$)	FE_{NH3}	Reference
P-TiO_2/TP	0.1 M Na_2SO_4 (0.1 M NO_2^-)	560.8	90.6%@-0.6 V	[5]
CoB@TiO_2/TP	0.1 M Na_2SO_4 (400 ppm NO_2^-)	233.1	95.2%@−0.7 V	[6]
Ag@NiO/CC	0.1 M NaOH (0.1 M NO_2^-)	338.3	96.1%@-0.7 V	[7]
Ni_2P/NF	0.1 M PBS (200 ppm NO_2^-)	191.3	90.2±3.0% @-0.3 V	[8]
CF@Cu_2O	0.1 M PBS (0.1 M NO_2^-)	441.8	94.2% @-0.6 V	[9]
MoS_2 NSs	0.5 M Na_2SO_4 (0.1 M NO_2^-)	528.8	93.52% @-0.5 V	[10]
Ni-TiO_2/TP	0.1 M NaOH (0.1 M NO_2^-)	380.27	94.89% @-0.5 V	[11]
NiS_2@TiO_2/TM	0.1 M NaOH (0.1 M NO_2^-)	485.4	92.1% @-0.5 V	[12]
ITO@TiO_2/TP	0.5 M $LiClO_4$ (0.1 M NO_2^-)	411.3	82.6% @-0.5 V	[13]
am-MoO_3	0.5 M Na_2SO_4 (0.1 M NO_2^-)	480.4	94.8% @-0.6 V	This work

References

[1]. P. Li, Z. Jin, Z. Fang and G. Yu, *Energy Environ. Sci.*, 2021, **14**, 3522-3531.

[2]. G. W. Watt and J. D. Chrisp, *Anal. Chem.*, 1952, **24**, 2006-2008.

[3]. K. Chen, Y. Zhang, J. Xiang, X. Zhao, X. Li and K. Chu, *ACS Energy Lett.*, 2023, **8**, 1281-1288.

[4]. Y. Li, S. Zhang, W. Xu, C. Jiang, L. Shao, S. Wang and J. Wang, *J. Mater. Chem. A*, 2023, **11**, 4000-4006.

[5]. L. Ouyang, X. He, S. Sun, Y. Luo, D. Zheng, J. Chen, Y. Li, Y. Lin, Q. Liu, A. M. Asiri and X. Sun, *J. Mater. Chem. A*, 2022, **10**, 23494-23498.

[6]. L. Hu, D. Zhao, C. Liu, Y. Liang, D. Zheng, S. Sun, Q. Li, Q. Liu, Y. Luo, Y. Liao, L. Xie and X. Sun, *Inorg. Chem. Front.*, 2022, **9**, 6075-6079.

[7]. Q. Liu, G. Wen, D. Zhao, L. Xie, S. Sun, L. Zhang, Y. Luo, A. Ali Alshehri, M. S. Hamdy, Q. Kong and X. Sun, *J. Colloid Interf. Sci.*, 2022, **623**, 513-519.

[8]. G. Wen, J. Liang, L. Zhang, T. Li, Q. Liu, X. An, X. Shi, Y. Liu, S. Gao, A. M. Asiri, Y. Luo, Q. Kong and X. Sun, *J. Colloid Interf. Sci.*, 2022, **606**, 1055-1063.

[9]. Q. Chen, X. An, Q. Liu, X. Wu, L. Xie, J. Zhang, W. Yao, M. S. Hamdy, Q. Kong and X.

Sun, *Chem. Commun.*, 2022, **58**, 517-520.

[10]. L. Yi, P. Shao, H. Li, M. Zhang, X. Peng, K. Chen, X. Liu and Z. Wen, *J. Power Sources*, 2023, **559**, 232668.

[11]. Z. Cai, C. Ma, D. Zhao, X. Fan, R. Li, L. Zhang, J. Li, X. He, Y. Luo, D. Zheng, Y. Wang, B. Ying, S. Sun, J. Xu, Q. Lu and X. Sun, *Mater. Today Energy*, 2023, **31**, 101220.

[12]. X. He, L. Hu, L. Xie, Z. Li, J. Chen, X. Li, J. Li, L. Zhang, X. Fang, D. Zheng, S. Sun, J. Zhang, A. Ali Alshehri, Y. Luo, Q. Liu, Y. Wang and X. Sun, *J. Colloid Interf. Sci.*, 2023, **634**, 86-92.

[13]. S. Li, J. Liang, P. Wei, Q. Liu, L. Xie, Y. Luo and X. Sun, *eScience*, 2022, **2**, 382-388.